Paleoceanography and Paleoclimatology

RESEARCH ARTICLE
10.1002/2017PA003313

Modeled Influence of Land Ice and CO_2 on Polar Amplification and Paleoclimate Sensitivity During the Past 5 Million Years

L. B. Stap[1,2], R. S. W. van de Wal[2], B. de Boer[2], P. Köhler[1], J. H. Hoencamp[2], G. Lohmann[1], E. Tuenter[3], and L. J. Lourens[4]

[1]Alfred-Wegener-Institut, Helmholtz-Zentrum für Polar- und Meeresforschung, Bremerhaven, Germany, [2]Institute for Marine and Atmospheric Research Utrecht, Utrecht, Netherlands, [3]Royal Netherlands Meteorological Institute (KNMI), De Bilt, Netherlands, [4]Department of Earth Sciences, Faculty of Geosciences, Utrecht University, Utrecht, Netherlands

Key Points:
- Polar amplification and paleoclimate sensitivity (*S*) are intimately linked over the past 5 Myr
- Similar radiative forcing strength by land ice and CO_2 changes has different effects on polar amplification and *S*
- Toward colder climates, northern polar amplification increases, causing southern polar amplification to decrease

Supporting Information:
- Supporting Information S1

Correspondence to:
L. B. Stap,
lennert.stap@awi.de

Citation:
Stap, L. B., van de Wal, R. S. W., de Boer, B., Köhler, P., Hoencamp, J. H., Lohmann, G., et al. (2018). Modeled influence of land ice and CO_2 on polar amplification and paleoclimate sensitivity during the past 5 million years. *Paleoceanography and Paleoclimatology*, *33*, 381–394. https://doi.org/10.1002/2017PA003313

Received 21 DEC 2017
Accepted 19 MAR 2018
Accepted article online 26 MAR 2018
Published online 22 APR 2018

Abstract Polar amplification and paleoclimate sensitivity (*S*) have been the subject of many paleoclimate studies. While earlier studies inferred them as single constant parameters of the climate system, there are now indications that both are conditioned by the type of forcing. Moreover, they might be affected by fast feedback mechanisms that have different strengths depending on the background climate. Here we use the intermediate complexity climate model CLIMBER-2 to study the influence of land ice and CO_2 on polar amplification and *S*. We perform transient 5-Myr simulations, forced by different combinations of insolation, land ice, and CO_2. Our results provide evidence that land ice and CO_2 changes have different effects on temperature, both on the global mean and the meridional distribution. Land ice changes are mainly manifested in the high latitudes of the Northern Hemisphere. They lead to higher northern polar amplification, lower southern polar amplification, and lower *S* than more homogeneously distributed CO_2 forcing in CLIMBER-2. Furthermore, toward colder climates northern polar amplification increases and consequently southern polar amplification decreases, due to the albedo-temperature feedback. As an effect, a global average temperature change calculated from high-latitude temperatures by using a constant polar amplification would lead to substantial errors in our model setup. We conclude that to constrain feedback strengths and climate sensitivity by paleoclimate data, the underlying forcing mechanisms and background climate states have to be taken into consideration.

1. Introduction

Equilibrium climate sensitivity (ECS) is a metric used to compare the different global temperature responses to a CO_2 doubling with respect to the preindustrial (PI) global reference temperature, thus $ECS = T_{glob}(2 \times CO_2) - T_{glob}(PI)$. It incorporates the total strength of the Planck response, as well as the fast feedbacks, for example, through snow, sea ice, lapse rate, clouds, and water vapor changes. The range in ECS shown by modern climate models in the CMIP5 project is 1.9 to 4.4 K per CO_2 doubling (Vial et al., 2013). Paleoclimate data can potentially be used to constrain this parameter (e.g., Covey et al., 1996; Edwards et al., 2007). However, real world paleotemperatures are affected by processes other than CO_2 changes, such as land ice, vegetation, and dust changes. To compensate for their effect, the induced global mean radiative forcing (ΔR) from all processes can be added up and used as a normalization for the temperature response (ΔT). This leads to the definition of $S = \Delta T/\Delta R$, also called paleoclimate sensitivity (PALAEOSENS Project Members, 2012). One obtains ECS out of *S* by multiplying *S* by 3.7 W/m^2, the radiative forcing related to a CO_2 doubling (Myhre et al., 1998). Using this approach, a data-based compilation showed a range in *S* of 0.6 to 1.3 K · W^{-1} m^2, which is equivalent to an ECS of 2.2 to 4.8 K (PALAEOSENS Project Members, 2012). However, this result relies on the assumption that radiative forcing caused by different processes leads to the same temperature response. Multiple studies have indicated that this is not the case, as different processes lead to different distributions of radiative forcing in the atmosphere (e.g., Bintanja et al., 1997; Hansen et al., 2005; Stuber et al., 2005; Yoshimori et al., 2011). For instance, radiative forcing caused by changes in long-lived greenhouse gases (GHGs) is fairly equally distributed over the globe, while land ice-induced albedo changes are mainly manifested in high latitudes. Therefore, the resulting meridional distribution of temperature perturbations will be different. Indeed, a study using a set of snapshot simulations over the last glacial cycle showed a dependency of polar amplification on the forcing processes (Singarayer & Valdes, 2010). In addition, the strength

of the Planck response and fast responses (or feedbacks) may vary between regions, leading to different temperature responses to the same global radiative forcing. As a result, the spatial pattern of the radiative forcing affects not only the meridional distribution but also the global mean of the temperature response (Bates, 2012; Armour et al., 2013). Moreover, when using either modeled or geological data from different time slices (e.g., Crucifix, 2006; Hargreaves et al., 2012; Schneider von Deimling et al., 2006; Schmittner et al., 2011), the possibility that S changes over time depending on the background climate is ignored, as indicated by, for example, Kutzbach et al. (2013), Meraner et al. (2013), Von der Heydt et al. (2014), Martínez-Botí et al. (2015), Köhler et al. (2015), and Friedrich et al. (2016). More information is required on how S and polar amplification depend on the forcing processes, and how they evolve over time. One way to progress is to study long-term transient climate simulations capturing long-term changes in forcing, and distinguishing between the effects of radiative forcing caused by the different processes involved. Unfortunately, long ($\sim 10^5$ to 10^6 years) integrations of state-of-the-art climate models, such as general circulation models (GCMs) and Earth system models, are currently not feasible due to limited computer power. This gap can be filled by using models of reduced complexity (Claussen et al., 2002; Stap et al., 2017).

In this study, we perform transient 5-Myr simulations of CLIMBER-2, a climate model of intermediate complexity (EMIC; Petoukhov et al., 2000). Different combinations of land ice, CO_2, and insolation changes are used as input for the model. We disentangle the results to obtain the pure contributions of CO_2 and land ice changes, as well as their synergy, to polar amplification and S. For conceptual understanding, we compare these CLIMBER-2 results to those of a separate simple linearized climate model based on the top-of-atmosphere energy budget (based on Bates, 2012). Finally, we discuss our results and their implications for the interpretation of high-latitude proxy data and the use of paleoclimate data to constrain climate models. A list of used variables, parameters, and abbreviations is contained in section S1 in the supporting information.

2. Models and Methods

2.1. CLIMBER-2

We use the EMIC CLIMBER-2 in the setup described by Petoukhov et al. (2000) and Ganopolski et al. (2001). CLIMBER-2 contains atmospheric, ocean, and terrestrial components. The atmosphere is represented by a 2.5-dimensional statistical-dynamical model with a 10° latitudinal, a ~51° longitudinal resolution (seven boxes in zonal direction), and a single-day time step. The prescribed vertical structure has 10 vertical levels for the calculation of circulation, temperature, and humidity, and 16 levels for long-wave radiative fluxes. The terrestrial model used in CLIMBER-2 is VECODE (Brovkin et al., 1997). This component determines the potential vegetation of every grid cell based on the temperature and precipitation, using a time step of 1 year. CLIMBER-2 further entails a three-basin ocean model based on Stocker et al. (1992). It describes the zonally averaged flow of water, as well as the evolution of temperature and salinity in the Atlantic, Indian, and Pacific basins, which are connected through the Southern Ocean. The time step is 5 days and the latitudinal resolution is 2.5°. The ocean contains 20 unevenly distributed vertical levels. Sea ice thickness and extent are calculated using a thermodynamic scheme. CLIMBER-2 compares favorably to GCMs in simulating present-day climate (Ganopolski et al., 2001; Petoukhov et al., 2000). Its low computational cost makes it well suited for paleoclimate research on long time scales. In earlier research, it has, for instance, been deployed to simulate the Pleistocene (Ganopolski & Calov, 2011), the Pliocene (Willeit et al., 2015), and the last glacial cycle (Robinson et al., 2011). Recently, the model has been used to design a critical insolation-CO_2 relation for diagnosing the inception of Northern Hemispheric glaciation (Ganopolski et al., 2016).

Here we force the climate model by data on insolation, land ice distribution, and CO_2 concentrations. To calculate insolation, we use the orbital solution of Laskar et al. (2004). The land ice forcing is taken from a 5-Myr run using the 3-D ice sheet model ANICE. In this run, land ice was forced by Northern Hemispheric temperatures obtained from benthic $\delta^{18}O$ (Lisiecki & Raymo, 2005) using the inverse technique described in De Boer et al. (2013; Figure 1a). This yields geographically specific land ice extent and thickness of the ice sheets in the Northern Hemisphere and the Antarctic ice sheet. Here we use an earlier realization of the land ice simulation from De Boer et al. (2014), with slightly different settings for the ice flow enhancement and mass balance parameters (see De Boer et al., 2013). The published results could not be used, since the CLIMBER-2 runs were started before finalization of that study. A comparison between the radiative forcing used in this study and the one derived in Köhler et al. (2015) from the final result of De Boer et al. (2014) is shown in Figure S1a. In our setup, ice volume variability influences the land albedo as well as the surface height, but not the ocean salinity.

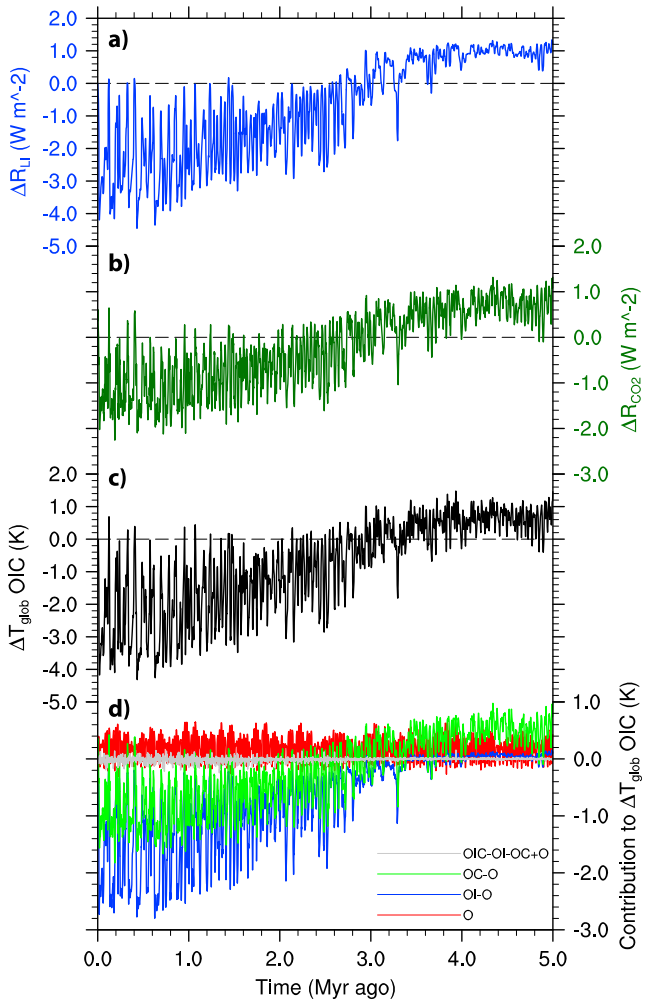

Figure 1. Overview of the radiative forcing perturbations with respect to preindustrial in the CLIMBER-2 runs (a, b) and of the resulting global temperature perturbations (c, d). (a) Radiative forcing perturbations by land ice changes, obtained from an ANICE simulation. (b) Radiative forcing perturbations by CO_2 changes, obtained from the approach by Van de Wal et al. (2011). (c) Global temperature perturbations in the OIC run (ΔT_{glob} OIC). (d) Contributions from orbital (O; red), land ice (OI-O; blue), CO_2 (OC-O; green) changes and the synergy of the latter two (OIC-OI-OC+O; gray) to the global temperature perturbations in the OIC run.

We use CO_2 concentrations from an updated version of the proxy data composition of Van de Wal et al., 2011 (2011; Figure 1b). This composition was originally constructed by inferring an instantaneous log-linear relation between the polar temperatures derived by De Boer et al. (2010) and an assemblage of CO_2 proxy data. The updated record is obtained using the same approach, but now based on the temperature simulation belonging to the ice sheet simulation used in CLIMBER-2 (Figure S1b). We use this CO_2 record, because it is continuous and mutually consistent with the ice sheet configuration, since both are based on the same temperature simulation. Proxy-based CO_2 input could in principal also be used, but this will not affect the qualitative behavior of the model, which is studied here. Non-CO_2 GHGs are not taken into account.

2.2. Forcing and Analysis

We perform four transient climate runs over the past 5 Myr (Table 1). In one run, we only vary insolation (O). We further vary either land ice (OI) or the CO_2 concentration (OC) in two more runs. In a fourth run, we vary all the input variables (OIC). The input that is not varied is kept constant at PI levels. Following Stein and Alpert (1993), we assess the effect of land ice from the difference between the OI and O runs (OI-O) and that of CO_2 concentrations from OC-O. The synergy of, or interaction among, ice volume and CO_2 changes is obtained from OIC-OI-OC+O. Because this synergy term in our results is very small (see section 3.2), the difference between the approach to disentangle contributions we adopt here (Stein & Alpert, 1993) and the approach more recently proposed by Lunt et al. (2012) is negligible. Throughout this paper, we analyze the output of CLIMBER-2 after averaging to 1,000-year temporal resolution.

To measure polar amplification, we use the relation between temperature differences from preindustrial values of the high-latitude regions (30–90°N and 30–90°S), and the global average. This is a widely adopted way to express polar amplification (cf. Masson-Delmotte et al., 2006; Singarayer & Valdes, 2010). By calculating the slope of a least squares linear fit ($\Delta T_{NH/SH} = c + f_{NH/SH} \times \Delta T_{glob}$) between these time series, we quantify the average polar amplification $f_{NH/SH}$, such that unity of $f_{NH/SH}$ means polar temperatures vary equally strong as global temperatures. Here c represents a very minor offset. We study specific paleoclimate sensitivity (S) by analyzing the relation between radiative forcing perturbations (ΔR), and global temperature differences (ΔT_{glob}) from preindustrial values (e.g., Friedrich et al., 2016; Köhler et al., 2015, 2017; Martínez-Botí et al., 2015; PALAEOSENS Project Members, 2012; Von der Heydt et al., 2014, 2016). Likewise as for the polar amplification, a least squares linear fit provides the average S. To be consistent with earlier studies (e.g., Köhler et al., 2010, 2015, 2017), we calculate the radiative forcing by CO_2 and land ice albedo changes by applying the energy balance scheme of Köhler et al. (2010). The radiative forcing by CO_2 (ΔR_{CO2}) follows from Myhre et al. (1998):

$$\Delta R_{CO2} = 5.35\,\mathrm{W\,m^2} \times \ln(CO_2/CO_{2,REF}), \quad (1)$$

Table 1
Description of the CLIMBER-2 Runs Performed Over the Past 5 Myr

Run	Orbital forcing	Ice volume forcing	CO_2 forcing
O	Laskar et al. (2004)	PI configuration	280 ppm
OI	Laskar et al. (2004)	ANICE simulation	280 ppm
OC	Laskar et al. (2004)	PI configuration	approach by Van de Wal et al. (2011)
OIC	Laskar et al. (2004)	ANICE simulation	approach by Van de Wal et al. (2011)

where $CO_{2,\,REF}$ is the preindustrial value of 278 ppm. The radiative forcing by land ice changes (ΔR_{LI}) is calculated per 10° latitudinal band i, and thereafter summed over all 18 bands:

$$\Delta R_{LI} = \sum_{i=1}^{18} \frac{-I_S(i) \times \Delta A_{LI}(i) \times \Delta\alpha}{A_{Earth}}, \tag{2}$$

where ΔA_{LI} is the land ice area perturbation from preindustrial, A_{Earth} the total area of the Earth, and $\Delta\alpha = 0.55$ is the difference in albedo between ice (sheets or shelves) and bare ground or open ocean. The annual mean insolation at the top of the atmosphere (I_{TOA}) is reduced by absorption ($a = 0.2$) and reflection ($\alpha_A = 0.212$) within the atmosphere, to calculate local surface insolation $I_S(i)$:

$$I_S(i) = I_{TOA}(i) \times (1 - (\alpha_A + a)). \tag{3}$$

Although regionally of importance, global radiative forcing changes caused by insolation are an order of magnitude smaller than the forcing changes caused by land ice and CO_2 (Köhler et al., 2010), and therefore neglected in this study. Total radiative forcing ($\Delta R_{CO2,LI}$) is obtained by adding the contributions of land ice and CO_2 changes, so that our calculated $S_{CO2,LI} = \frac{\Delta T_{glob}}{\Delta R_{CO2,LI}}$, similar to the definition in PALAEOSENS nomenclature. However, a direct comparison with $S_{CO2,LI}$ from data-based approaches is hindered by the fact that we neglect various processes that are known to be important for global temperature change, such as non-CO_2 GHGs and dust changes. This also means we are not in the position to provide a new estimate for S. Instead, our aim here is to disentangle the influence of land ice and CO_2 on this quantity, and to explain any background state dependence that occurs in our model.

2.3. Linearized Energy Balance Climate Model

To gain conceptual insight, we perform some independent experiments using a conceptual linearized box model based on the top-of-atmosphere energy budget. Basically, it is a numerical implementation of Model B from Bates (2012), generalized to three boxes. These three boxes represent the high-latitude regions and the tropical region, each being assumed to cover one third of the area of the globe; thus, the dividing latitude ϕ between the boxes is such that $\sin(\phi) = \pm 1/3$. This setup differs from the boundaries we use to analyze polar amplification in CLIMBER-2, where ϕ is chosen such that $\sin(\phi) = \pm 1/2$. All regions are characterized by a unit area radiative response coefficient (b_{NH}, b_{SH}, and b_{trop} in $W \cdot m^{-2} \cdot K^{-1}$), which dictates how strong the temperature in that region reacts to radiative perturbations. These coefficients capture the Planck response, as well as the fast feedbacks through snow, sea ice, lapse rate, clouds, and water vapor changes. The stronger these feedbacks, the smaller the response coefficient, and the larger the temperature change becomes. The atmospheric heat transport between the boxes is determined by the temperature differences between them multiplied by coefficients for exchange between the tropics and northern high-latitude region (d_{NH} in $W \cdot m^{-2} \cdot K^{-1}$), and between the tropics and southern high-latitude region (d_{SH}). In more sophisticated models, these coefficients can vary between different background climate states (Caballero & Langen, 2005). However, for simplicity we keep them constant here and compare runs using different values to analyze the effect that strength variations may cause. In the model, radiative forcing perturbations in each box (ΔR_{NH}, ΔR_{SH}, and ΔR_{trop}) yield temperature responses in the same box (ΔT_{NH}, ΔT_{SH}, and ΔT_{trop}) and heat transport between the different boxes:

$$\Delta R_{NH} = b_{NH}\Delta T_{NH} - d_{NH}(\Delta T_{trop} - \Delta T_{NH}), \tag{4}$$

$$\Delta R_{SH} = b_{SH}\Delta T_{SH} - d_{SH}(\Delta T_{trop} - \Delta T_{SH}), \tag{5}$$

$$\Delta R_{trop} = b_{trop}\Delta T_{trop} + d_{NH}(\Delta T_{trop} - \Delta T_{NH}) + d_{SH}(\Delta T_{trop} - \Delta T_{SH}). \tag{6}$$

The model solves these equations linearized in ΔT, which provides the steady state response of temperature to radiative perturbations in the different regions:

$$\Delta T_{NH} = \frac{1}{\Gamma}\left(\frac{d_{NH}}{\beta} \times \Delta R_{trop} + \left(\frac{(d_{NH})^2}{\beta^2} + \frac{\Gamma}{\beta}\right) * \Delta R_{NH} + \frac{d_{NH} \times d_{SH}}{\beta \times \gamma} \times \Delta R_{SH}\right) \tag{7}$$

$$\Delta T_{SH} = \frac{1}{\Gamma}\left(\frac{d_{SH}}{\gamma} \times \Delta R_{trop} + \frac{d_{NH} \times d_{SH}}{\beta \times \gamma} \times \Delta R_{NH} + \left(\frac{(d_{SH})^2}{\gamma^2} + \frac{\Gamma}{\gamma}\right) \times \Delta R_{SH}\right) \tag{8}$$

$$\Delta T_{trop} = \frac{1}{\Gamma}\left(\Delta R_{trop} + \frac{d_{NH}}{\beta} \times \Delta R_{NH} + \frac{d_{SH}}{\gamma} \times \Delta R_{SH}\right) \tag{9}$$

Table 2
Results of the Conceptual Model Runs: Paleoclimate Sensitivity (S) and Polar Amplification for the Northern (f_{NH}) and Southern (f_{SH}) Hemispheric High-Latitude Regions

		$b_{NH} = 1.5$ $b_{SH} = 1.5$ $b_{trop} = 1.5$	$b_{NH} = 1.0$ $b_{SH} = 1.0$ $b_{trop} = 1.5$	$b_{NH} = 0.5$ $b_{SH} = 1.0$ $b_{trop} = 1.5$
Homogeneous	S (K · W^{-1} · m^2)	0.66	0.86	1.02
	f_{NH}	1.00	1.01	1.07
	f_{SH}	1.00	1.01	0.97
Inhomogeneous	S (K · W^{-1} · m^2)	0.66	0.87	1.09
	f_{NH}	1.46	1.40	1.40
	f_{SH}	0.65	0.71	0.71

Note. The columns give settings for the radiative response coefficients ($b_{NH,SH,trop}$ in W · m^{-2} · K^{-1}), the rows distinguish between homogeneous ($\Delta R_{NH} = \Delta R_{SH} = \Delta R_{trop} = 4.0$ W/m^{-2}) and inhomogeneous ($\Delta R_{NH} = 12.0$ W/m^{-2}, $\Delta R_{SH} = \Delta R_{trop} = 0$ W/m^{-2}) forcing. All runs are executed using the same atmospheric heat transport coefficients ($d_{NH,SH} = 4.0$ W · m^{-2} · K^{-1}). The results in blue are the same as those in Table 3.

where $\alpha = b_{trop} + d_{NH} + d_{SH}$, $\beta = b_{NH} + d_{NH}$, $\gamma = b_{SH} + d_{SH}$, and $\Gamma = \alpha - \frac{(d_{NH})^2}{\beta} - \frac{(d_{SH})^2}{\gamma}$. We determine polar amplification (f_{NH}, f_{SH}) as the ratios between high-latitude and global ($\Delta T = (\Delta T_{NH} + \Delta T_{SH} + \Delta T_{trop})/3$) temperature response. S is obtained by dividing the global temperature response by the global radiative perturbation ($\Delta R = (\Delta R_{NH} + \Delta R_{SH} + \Delta R_{trop})/3$). In the runs with homogeneous radiative perturbations, we set $\Delta R_{NH} = \Delta R_{SH} = \Delta R_{trop} = 4.0$ W/m^{-2}. In the runs with inhomogeneous forcing, the radiative perturbation is confined to the northern polar region: $\Delta R_{NH} = 12.0$ W/m^{-2}, $\Delta R_{SH} = \Delta R_{trop} = 0$ W/m^{-2}. Parameter settings for identical and differing radiative responses in the different regions (Table 2), as well as zero ($d = 0$ W · m^{-2} · K^{-1}) to infinite ($d = \infty$ W · m^{-2} · K^{-1}) atmospheric heat transport (Table 3), are used. These settings are chosen to yield realistic results for S. The simulations will be used for conceptual understanding of the CLIMBER-2 results, based on simple energy balance considerations.

3. Results

3.1. Global Temperature

Solely taking insolation variability into account in CLIMBER-2 (Figure 1d; scenario O), the mean global temperature varies only by 0.5 K during the whole simulated period. In the other scenarios where more input variables are varied, changes in global temperatures are larger (Figures 1c and 1d). During the Pliocene period (5 to 2.7 Myr ago), land ice variations are weak. Consequently, CO_2 is the dominant factor controlling global surface air temperature (Figure 1d; OC-O). Global mean temperature in the OIC run is up to 1.2 K warmer

Table 3
As Table 2

		$d_{NH} = 0$ $d_{SH} = 0$	$d_{NH} = 4.0$ $d_{SH} = 4.0$	$d_{NH} = 8.0$ $d_{SH} = 4.0$	$d_{NH} = \infty$ $d_{SH} = \infty$
Homogeneous	S (K · W^{-1} · m^2)	1.22	1.02	1.01	1.00
	f_{NH}	1.64	1.07	1.04	1.00
	f_{SH}	0.82	0.97	0.99	1.00
Inhomogeneous	S (K · W^{-1} · m^2)	2.00	1.09	1.05	1.00
	f_{NH}	3.00	1.40	1.25	1.00
	f_{SH}	0.00	0.71	0.78	1.00

Note. The columns give settings for the atmospheric heat transport coefficients ($d_{NH,SH}$ in W · m^{-2} · K^{-1}), the rows distinguish between homogeneous ($\Delta R_{NH} = \Delta R_{SH} = \Delta R_{trop} = 4.0$ W/m^{-2}) and inhomogeneous ($\Delta R_{NH} = 12.0$ W/m^{-2}, $\Delta R_{SH} = \Delta R_{trop} = 0$ W/m^{-2}) forcing. All runs are executed using the same radiative response coefficients ($b_{NH} = 0.5$, $b_{SH} = 1.0$, $b_{trop} = 1.5$ W · m^{-2} · K^{-1}). The results in blue are the same as those in Table 2.

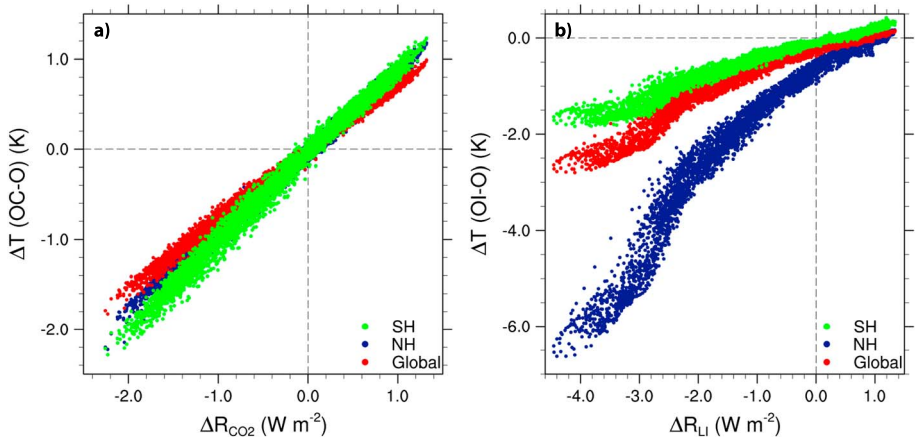

Figure 2. (a) The relation between radiative forcing by CO_2 changes (ΔR_{CO2}) and temperature differences (ΔT) between CLIMBER-2 runs OC and O and (b) radiative forcing by land ice changes (ΔR_{LI}) and temperature differences (ΔT) between OI and O. For the temperature differences, shown are the whole globe (red), the northern (30–90°N; blue) and the southern high-latitude region (30–90°S; green). The blue dots are partly overlain by the red and green dots. Note the differing axis scales.

during the Pliocene than at the last time step, which represents PI climate (Figure 1c). Because the Pliocene CO_2 levels used here are lower than the 405 ppm used in PlioMIP (Figure 1b), this temperature increase is smaller than the 1.84 to 3.60 K range calculated by that GCM ensemble (Experiment 2 in Haywood et al., 2013). Recent model studies show that the CO_2 level could have been even higher than 405 ppm during the Pliocene (Stap et al., 2016; Willeit et al., 2015), but the exact concentration remains under debate as some proxy data indicate a lower concentration (Badger et al., 2013; Martínez-Botí et al., 2015). Rather than making an accurate reconstruction of climate, we focus on the qualitative behavior of the model. At around 2.8 Myr ago, glacial inception in the Northern Hemisphere causes ice volume variations to become much larger (Figure 1d; OI-O). From then on they exert a larger control on surface air temperature than CO_2. Global temperature decreases to about 4 K below PI during the last four glacial cycles.

3.2. Polar Amplification

Radiative forcing caused by CO_2 changes is approximately spatially homogeneous. It leads to a weak polar amplification in CLIMBER-2, as the temperature perturbations are slightly larger in the high-latitude regions than in the tropics (Figure 2a; OC-O). This can be understood conceptually from the energy balance model, by the high-latitude regions having a smaller radiative response coefficient than the low latitudes (Table 2), which is most probably a result of snow and sea ice changes. For the same reason, the temperature response is stronger in the southern than in the northern high latitudes.

Land ice changes predominantly affect the Northern Hemispheric high-latitude region. From energy balance considerations, this should lead to increased polar amplification in the Northern Hemisphere in the physically realistic case of finite atmospheric heat transport (Tables 2 and 3). Indeed, also in CLIMBER-2 the temperature response is much stronger in the Northern Hemisphere than elsewhere (Figure 2b; OI-O). Besides changing albedo, there is also a contribution of the changing orography due to the ice sheets dynamics to the polar amplification in the northern high latitudes (e.g., Romanova et al., 2006). The northern high-latitude region contributes more to the global response, which diminishes the relative contribution of the southern high-latitude region, and hence southern polar amplification. The effect of the Northern Hemisphere on southern polar amplification is hence in part caused by the definition of polar amplification as the ratio of high-latitude temperatures over the global average. However, increased cooling in the Northern Hemisphere is partly compensated for by increased heat transport from the low-latitude area, which cools the tropics. Therefore, the same interrelation is found when polar amplification is expressed as the ratio of high-latitude temperature change over tropical temperature change, albeit less pronounced. Comparing the polar amplification in the different CLIMBER-2 runs, we see that northern polar amplification is indeed stronger in the OI run than in the OC run (slopes of the blue and green dots in Figure 3a). For southern polar amplification, it is the other way around (slopes in Figure 3b). Polar amplification is on average 2.2 and 0.8 in the OI run for the Northern and Southern Hemispheres, respectively, and in the OC run 1.3 for both hemispheres. The synergy

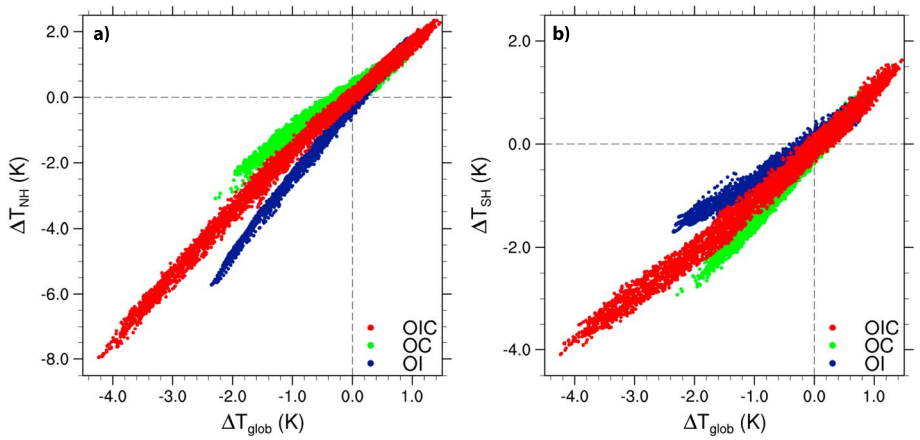

Figure 3. The relation between global (ΔT_{glob}) and high-latitude temperature anomalies for the (a) Northern Hemisphere (ΔT_{NH}) and (b) Southern Hemisphere (ΔT_{SH}), in the OI (blue), OC (green), and OIC (red) CLIMBER-2 runs. Note the differing *y* axis scales.

of ice volume and CO_2 changes on temperature is only very small (Figure 1d; OIC-OI-OC+O). Therefore, the polar amplification factor in the OIC scenario is in-between the factors of the OI and OC scenarios: 1.8 for the Northern and 1.0 for the Southern Hemisphere.

3.3. Climate Sensitivity

The difference between the spatial distributions of the radiative forcing by ice volume and CO_2 changes also affects *S* (Figure 4a). In the more inhomogeneous case (OI), radiative forcing is confined to the high northern latitudes where the temperature response is larger (Figure 5). In this case, the energy balance model predicts increased *S* (Table 3). However, CLIMBER-2 simulates 42% smaller average $S(= S_{LI})$ in the OI run (0.47 K · W^{-1} · m^2) than $S(= S_{CO2})$ in the OC run (0.81 K · W^{-1} · m^2), the $S(= S_{CO2,LI})$ of the OIC run being in the middle (0.62 K · W^{-1} · m^2). This is due to albedo changes by snow being smaller on an ice sheet than on vegetation or bare ground, hence reducing their amplifying effect on temperature perturbations.

3.4. Nonlinearity

The $\Delta R_{CO2,LI}$ versus ΔT scatterplot of the CLIMBER-2 results contains a nonlinear relationship (Figure 4a), which is an indicator for state dependency in *S* (e.g., Köhler et al., 2015). For all scenarios, a second-order fit has a significantly larger coefficient of determination (r^2) than a linear fit. We use *F* tests based on the residual sum of squares to identify if the second-order polynomial is a better fit to the results than the linear one. The nonlinearity originates from the Northern Hemisphere, as there the temperature response increases toward colder climates (Figure 2a). Therefore, northern polar amplification grows, and consequently southern polar amplification declines (Figure 3). This behavior is not caused by increased inhomogeneity of the radiative

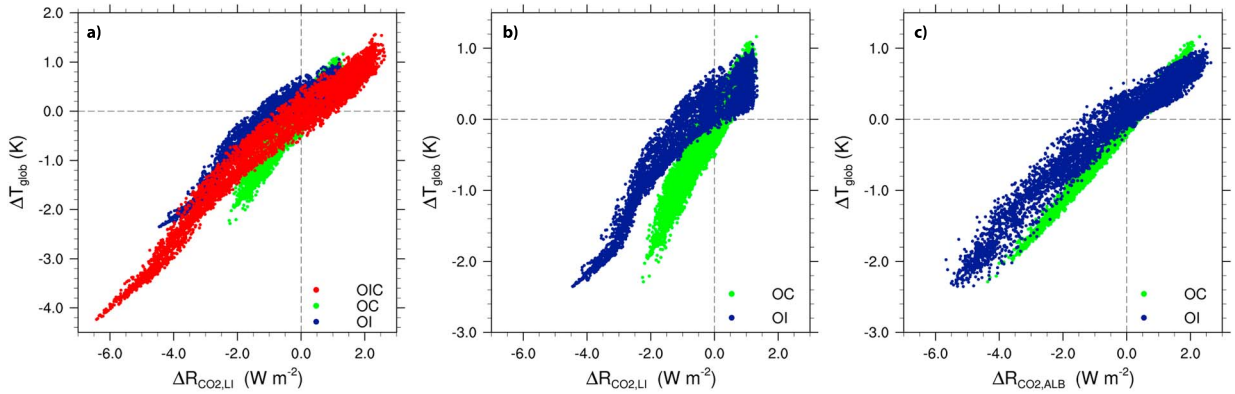

Figure 4. (a) The relation between radiative forcing ($\Delta R_{CO2,LI}$) and global temperature anomalies (ΔT_{glob}), in the OI (blue), OC (green), and OIC (red) CLIMBER-2 runs. (b) Same as (a), but only for the OI (blue), and OC (green) runs. (c) Same as (b) but using ΔR_{ALB} (equation (10)) instead of ΔR_{LI} (equation (4)) to calculate the radiative forcing ($\Delta R_{CO2,ALB}$). Note the differing *y* axis scales.

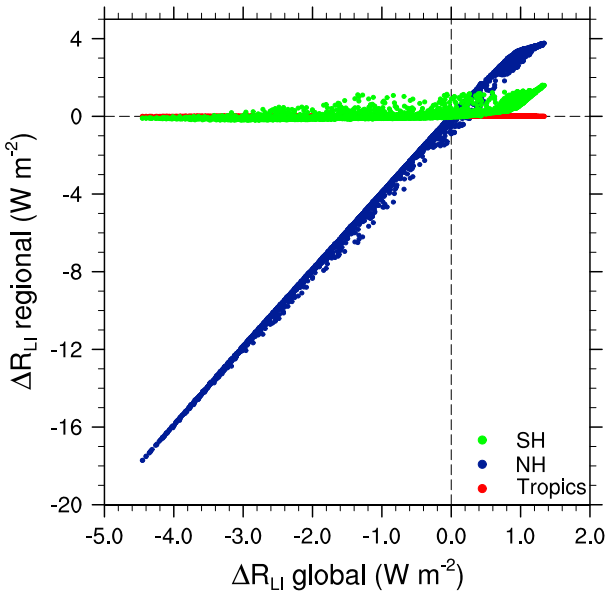

Figure 5. The relation between global and regional radiative forcing by land ice changes (ΔR_{LI}), for the northern (30–90°N) and southern (30–90°S) high-latitude regions and the tropical region (30°N–30°S) in CLIMBER-2.

forcing (Figure 5). Therefore, it is an effect of a increasing global temperature response to radiative forcing in the Northern Hemisphere. This response might be amplified by larger variations in albedo caused by vegetation, snow, and sea ice changes. As a check, we compensate S for this, by adding the total albedo change caused by all processes as a forcing in the calculation (ΔR_{ALB}):

$$\Delta R_{ALB} = \sum_{i=1}^{18} \frac{-I_S(i) \times A_i \times \Delta\alpha_{TOT}}{A_{Earth}}, \quad (10)$$

where A_i is the area of the latitudinal band and $\Delta\alpha_{TOT}$ the total surface albedo change determined from the CLIMBER-2 results. This term replaces ΔR_{LI} in the calculation of total radiative forcing (now $\Delta R_{CO2,ALB}$) and S. Calculated in this way, the relationship between $\Delta R_{CO2,ALB}$ and ΔT_{glob} is more linear. This implies that the nonlinearity of albedo changes in the Northern Hemisphere at lower temperatures is indeed the most important contributor to the state dependency in S (Figures 3, 4b, and 4c). The residual nonlinearity can, for instance, be caused by emissivity changes that are not accounted for by this albedo correction.

4. Discussion

4.1. Model Performance

Comparing our simulated temperature record to data-based approaches is hampered by the fact that we only take into account CO_2 changes. Our used GHG forcing is therefore smaller than in reality. Furthermore, we neglect other processes, such as dust changes, which could have an inhomogeneous effect on radiative forcing (e.g., Kohfeld & Harrison, 2001; Mahowald et al., 2006). Our results are therefore not intended to closely capture the evolution of climate over the past 5 Myr. Instead, we focus on the relative influences of land ice and CO_2 on polar amplification and S.

The global mean temperature difference between the Last Glacial Maximum (LGM; 20 kyr ago) and PI is −4.1 K in our fully coupled OIC run. Even with the lack of the processes mentioned above, this is in agreement with the -4.0 ± 0.8 K from a recent data reconstruction (Annan & Hargreaves, 2013). This agreement could either imply that the neglected processes only have a small impact or that their effects compensate each other. In addition, the latitudinal distribution of the LGM-PI difference is within the error margins, which represent zonally

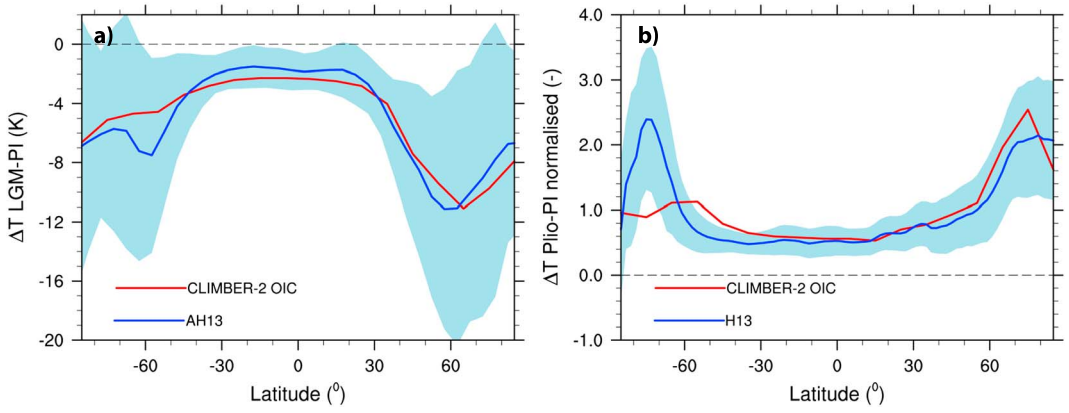

Figure 6. (a) Modeled difference in zonally averaged surface air temperature between Last Glacial Maximum and preindustrial (PI) for the OIC CLIMBER-2 run (red line), compared to the data reconstruction by Annan and Hargreaves (2013) (AH13; blue line with error margin). (b) Modeled difference in zonally averaged surface air temperature between 4524 kyr ago, a time with a 313 ppm CO_2 level and orbital settings comparable to present day, and PI for the OIC run (red line), compared to the Pliocene to PI difference calculated by the PlioMIP ensemble, Experiment 2 (Haywood et al., 2013) (H13; blue line with error margin). Both are normalized through a division by the mean global temperature perturbation.

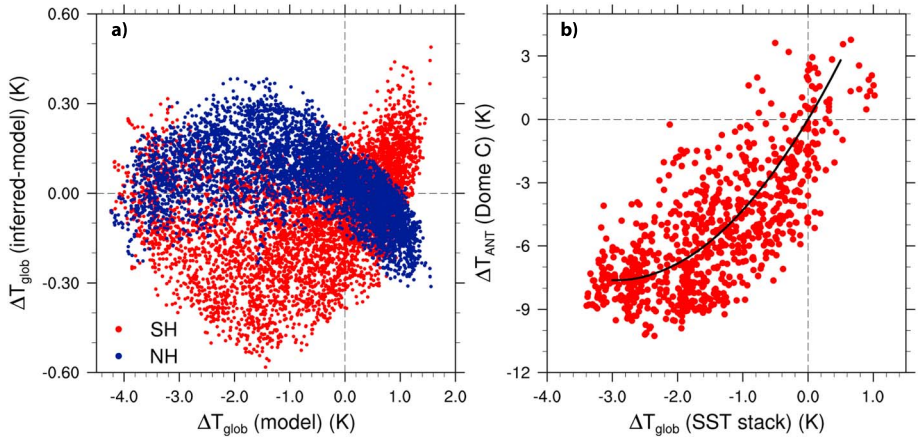

Figure 7. The relation between global mean temperature perturbations from preindustrial in the OIC CLIMBER-2 run calculated by the model [ΔT_{glob} (model)], and the difference between these and those inferred from dividing the high-latitude temperatures on the (a) Northern Hemisphere (blue) and the Southern Hemisphere (red), by the polar amplification factor obtained from the Last Glacial Maximum-preindustrial temperature difference (NH = 1.85, SH = 0.96), over the past 5 Myr. (b) The relation between proxy global mean temperature perturbations obtained from an sea surface temperature stack (Martínez-Botí et al., 2015), and the Dome C Antarctic temperature record (Jouzel et al., 2007), over the past 784 kyr. The black line is a second-order fit. Note the differing axis scales.

averaged uncertainty, coherent to Annan & Hargreaves (2013; Figure 6a). However, we somewhat underestimate cooling in the Southern Hemisphere, while we overestimate it in the tropics.

PlioMIP Experiment 2 calculates Pliocene temperature anomalies from PI using a GCM ensemble, with 405 ppm CO_2 and present-day insolation (Haywood et al., 2013). For a comparison, we use the difference between PI and 4,524 kyr ago, a time when orbital settings were comparable to present day and the CO_2 level was high at 313 ppm. However, because of the difference in CO_2, the temperature anomalies simulated here are smaller than those in PlioMIP. To compare the spatial pattern, we therefore normalize the results through a division by the global mean temperature change. The latitudinal distribution of the temperature difference looks similar to the LGM-PI difference, with underestimated Southern Hemispheric warming and overestimated tropical warming (Figure 6b). In this case, it is probably largely due to the use of different settings for the Antarctic ice sheet in our simulation. The Antarctic ice sheet simulated by ANICE has a larger area and higher surface elevation than the PRISM3 boundary conditions used in PlioMIP (Dowsett et al., 2010). Nonetheless, it is possible that the change of atmospheric heat transport toward the South is underestimated by CLIMBER-2.

4.2. Polar Amplification

The nonconstant polar amplification simulated by CLIMBER-2 affects the interpretation of high-latitude temperature perturbations in terms of global change. This becomes evident when we use the polar amplification factors obtained from the LGM-PI differences (1.85 for the Northern Hemisphere and 0.96 for the Southern Hemisphere) to estimate global temperature changes over the whole simulated period (Figures 7a and S2). The difference between these estimates and the actual modeled global temperature anomalies is determined by the product of the temperature anomaly and the error in polar amplification. The temperature anomaly is the lowest during glacial times comparable to PI. The error in polar amplification, however, is by construction the lowest at glacial times comparable to LGM and grows toward interglacial climates (Figure 3). Therefore, the maximum of the difference between inferred and actual modeled global temperature is obtained in-between interglacial and full glacial conditions. This approach of inferring global temperature changes overestimates them by up to 0.4 K maximally using Northern Hemispheric temperatures, while it underestimates them by up to 0.6 K using Southern Hemispheric temperatures. The spread in the obtained error as a function of the modeled global temperature anomaly is, however, substantial (Figure 7a). In addition, the exact values for the maximum differences depend on the chosen boundaries for the high-latitudes (30–90°). They will increase if the polar area is more confined to regions where the temperature variability is larger (see Figure 6).

Observing nonlinear polar amplification in geological data is difficult, since continuous records are scarce. Furthermore, proxies are influenced by the aforementioned processes we omit. Generally, they record temperature change at one specific location, which is possibly poorly represented by models due to the resolution.

Recently, a spatially weighted proxy reconstruction of global temperature from a multiproxy database of sea surface temperature (SST) point reconstructions was presented (Snyder, 2016). It was compared to a reconstruction of Antarctic temperature based on the deuterium isotope record of the EPICA Dome C ice core (Jouzel et al., 2007). This record has been suggested to be a proxy for global temperature anomalies when divided by a constant factor (Masson-Delmotte et al., 2006). Indeed, no sign of nonlinearity in the relation between global and polar temperature was found, although the errors are large (Figure 2a in Snyder, 2016). However, the relationship between the Antarctic proxy record and another global temperature proxy, which was obtained by stacking SST records (Martínez-Botí et al., 2015), gives a hint of nonlinearity (Figure 7b). A second-order fit through these data is significantly better (larger r^2) than a linear fit.

Most modeling studies focusing on long-term polar amplification using more sophisticated climate models are based on timeslice experiments (e.g., Goldner et al., 2014; Haywood et al., 2013; Holland & Bitz, 2003). Temporal variability in polar amplification cannot be extracted from this information. Performing snapshot simulations using a GCM, one earlier study evaluated polar amplification over the last glacial cycle (Singarayer & Valdes, 2010). They did not find a general relation between polar amplification on the Northern and Southern Hemispheres. From a conceptual perspective, a changing atmospheric heat transport coefficient could offset the variability in polar amplification (Table 3). Therefore, the CLIMBER-2 results are contingent on the parameterization of heat transport, and hence possibly model specific. More comprehensive model intercomparisons of transient simulations, such as the planned PMIP4 deglaciation experiments (Ivanovic et al., 2016), are needed to draw firm conclusions.

4.3. Climate Sensitivity

The global mean temperature difference between the LGM and PI is −2.2 K in the OI, and −1.9 K in the OC run. Since orbital variations have a negligible influence, this means that 54% of the cooling is due to ice sheets, and 46% due to CO_2 changes. This is within the broad range of previous model estimates (Figure 1 in Shakun, 2017). It is most comparable to Singarayer and Valdes (2010), but they also varied the GHG CH_4 and N_2O.

As our most important finding, we show a dependency of S on the type of forcing in CLIMBER-2; it is different in the OI than in the OC run. Conceptually, such a difference between the effects of spatially homogeneous and inhomogeneous forcings can be explained by regions having separate temperature responses to the same radiative forcing (Bates, 2012). The same behavior is also shown by many other studies using models of varying complexity (e.g., Bintanja et al., 1997; Stuber et al., 2005; Yoshimori et al., 2011), which sometimes have ozone as their spatially inhomogeneous forcing agent. It implies that it is difficult to derive a global average temperature change from a global average radiative forcing.

In addition, S is background state dependent in CLIMBER-2, as a result of changing strength of the albedo-temperature feedback in the Northern Hemisphere. This result is coherent with the findings of Pfister and Stocker (2017), who showed that in most EMICs S decreases when CO_2 concentrations are increased from PI to 4 × PI values. However, note that the evidence from GCMs is currently ambiguous, as some show increasing S with increasing forcing. State dependency of S is also found, but not explained, by a study using a hybrid model data approach (Friedrich et al., 2016). They calculated S over the past 784 kyr from a combination of a reconstructed SST record and results of the EMIC LOVECLIM. In their study, S decreases toward colder climates, which is opposite to our result. Their pure model results, however, show a linear relation between global atmospheric temperature anomalies and radiative forcing by land ice and GHG changes ($\Delta R_{GHG,LI}$; Figure 8a). Therefore, we deduce that the nonlinearity in the study of Friedrich et al. (2016) mainly stems from the reconstructed, rather than the modeled, global temperatures. Dust changes are not used to force the CLIMBER-2 and LOVECLIM simulation. However, in Figure 8b, we have added dust changes from the Dome C ice core (Köhler et al., 2010; Lambert et al., 2008) to the calculation of radiative forcing ($\Delta R_{GHG,LI,AE}$). This means that in this figure the global average temperature changed derived from the simulations are not in mutual agreement with the calculated forcing. Only after this somewhat artificial correction both LOVECLIM and CLIMBER-2 show decreasing S toward colder climates.

A recent paleo data analysis (Köhler et al., 2015) also found decreasing S toward colder climates. The difference between their result and ours is mainly generated by the global temperature records that are used, as can be deduced from the nonlinear relation between them. They determined global temperatures from the Northern Hemispheric temperature record of De Boer et al. (2014) by using a polar amplification factor that increased toward colder climates based on analysis of PMIP3 (ΔT_{g1} in Köhler et al., 2015, plotted against our ΔT_{glob} in Figure 8c). In Figure 8d, we show the relation between the original polar temperature records

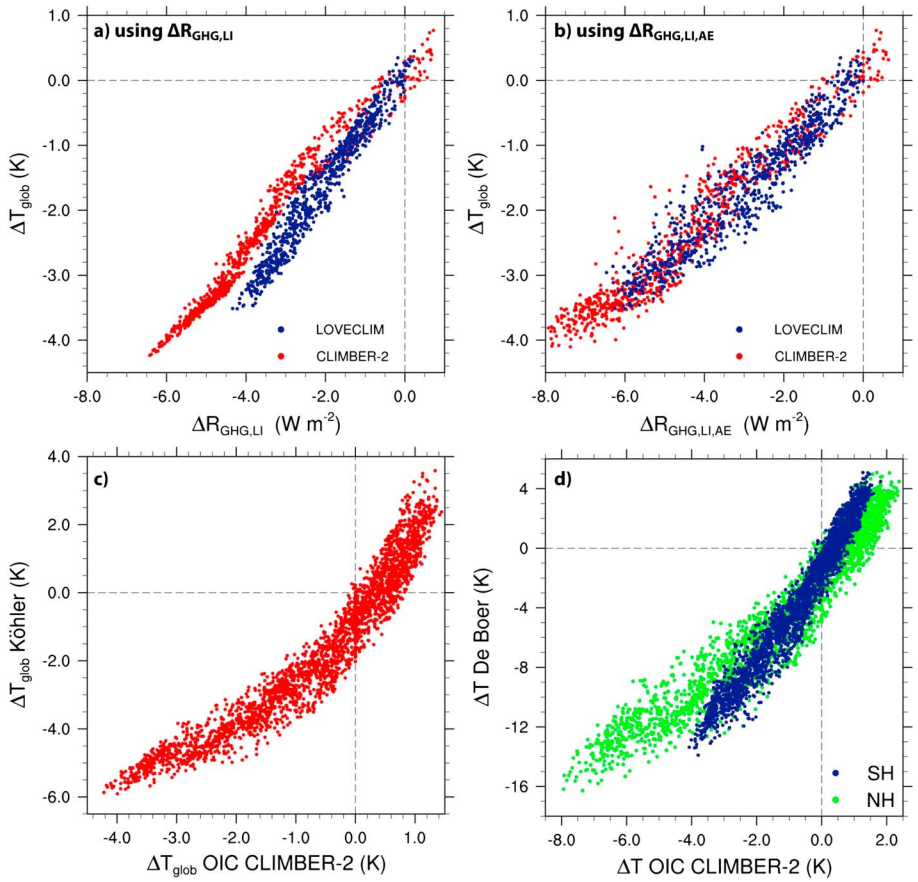

Figure 8. (a) The relation between radiative forcing by greenhouse gases and land ice changes ($\Delta R_{GHG,LI}$) and global temperature anomalies (ΔT_{glob}) over the past 784 kyr from the CLIMBER-2 OIC run (red) and from simulations with the climate model LOVECLIM (Friedrich et al., 2016) (blue). (b) Same as (a) but adding radiative forcing from dust changes to the total radiative forcing anomalies ($\Delta R_{GHG,LI,AE}$). (c) The relation between the global temperature anomalies in CLIMBER-2 run OIC and the global temperature anomaly record (ΔT_{g1}) derived in Köhler et al. (2015), over the past 5 Myr. The latter is obtained by dividing the temperature record of De Boer et al. (2014) by a polar amplification factor that linearly increases going from warm to cold conditions. (d) The relation between the northern (green) and southern (red) high-latitude temperature anomalies in CLIMBER-2 run OIC and the polar temperature anomaly records for the Northern and Southern Hemispheres from De Boer et al. (2014). Note the differing axis scales.

for the Northern and Southern Hemispheres of De Boer et al. (2014) and the high-latitude temperatures from CLIMBER-2. For the Southern Hemispheric temperatures (blue dots), this relation is more linear than for the Northern Hemispheric temperatures (green dots). Using the southern polar temperatures from De Boer et al. (2014), in combination with an appropriate polar amplification factor that decreases toward colder climates, could therefore lead to a different *S* result that is more similar to ours.

In short, *S* is strongly depending on the used global average temperature record. A way forward from here is to use more proxy-based temperature records in the analysis of *S*. Therefore, a more comprehensive temporal and spatial coverage of paleotemperature data is needed. Any mismatch between CLIMBER-2 results and data could be caused by omitted processes, such as dust changes, non-CO_2 GHGs or interactive coupling with an ice sheet model. In future modeling work, more processes should be included to obtain more reliable agreement with geological data.

5. Conclusions

Earlier work tried to constrain climate sensitivity from both modeled and observed paleoclimate data (e.g., Friedrich et al., 2016; Köhler et al., 2015; Martínez-Botí et al., 2015; Von der Heydt et al., 2014). To compensate for slow feedbacks like ice sheet changes, they added the induced radiative forcing by these processes to the radiative forcing by CO_2 changes. This result relies on the assumption that radiative forcing caused

by different processes leads to the same temperature response. However, analysis with a simple linearized energy balance climate model suggests that this does not hold when the spatial distribution of the radiative forcing differs (Bates, 2012). Therefore, the effects of land ice and CO_2 on both regional and global average temperature might be different in cases where their radiative forcings defined as global averages are the same.

Here we use 5-Myr transient runs of the EMIC CLIMBER-2 to analyze the separate and combined influences of land ice and CO_2 changes on polar amplification and paleoclimate sensitivity (S). Since our results are based on a single climate model and therefore model dependent, the quantitative conclusions should only be used to compare to results of other studies. In a qualitative sense, however, they are more likely to be robust. In CLIMBER-2, the tropics and the northern and southern high-latitude regions react with different strength to radiative forcing. This causes differing responses to spatially homogeneous and inhomogeneous radiative forcing, both of the global mean temperature and the meridional distribution. Therefore, the strength of polar amplification and *S* depends on the type of forcing. Ice volume changes lead on average to 77% higher northern polar amplification and 38% lower southern polar amplification than CO_2 changes. *S* is 42% lower in the case of ice volume changes, because albedo changes by snow and sea ice are less effective on ice sheets than on vegetation, sea, or bare ground. We conclude that a good distinction between different forcings is imperative when using paleoclimate data to constrain climate models. Since polar amplification and *S* are intimately linked, comprehensive temporal and spatial coverage of paleotemperature data could prove crucial to validate model results.

Furthermore, in CLIMBER-2 the strength of the albedo-temperature feedback, which is caused by all processes other than land ice changes, is not constant in time. This leads to increased *S* and northern polar amplification toward glacial climates, while southern polar amplification decreases. This would hamper inferring global means from high-latitude proxy temperature data. The CLIMBER-2 results suggest that a correction of up to 0.6 K has to be made when southern high-latitude records, such as ice cores, are used to estimate global mean temperatures. However, this result is highly dependent on how the boundaries for the high-latitude regions are chosen. Support from data and more sophisticated climate models for this nonlinear behavior is very scarce. More transient simulations of these models are therefore needed to analyze whether our findings can be corroborated, or else why this is not the case.

Acknowledgments
This paper contributes to PACES-II, the Helmholtz Research Programme of AWI, and to the gravity program "Reading the past to project the future," funded by the Netherlands Organisation for Scientific Research (NWO). L. B. Stap was funded by NWO Earth and Life Sciences (ALW), project 822.01.006. B. de Boer is funded by NWO Earth and Life Sciences (ALW), project 863.15.019. We thank Andrey Ganopolski for providing the CLIMBER-2 code and commenting on an early draft of the paper, and Tobias Friedrich for sharing data. The authors declare no conflict of interest. The model results presented in this paper are available online at https://doi.pangaea.de/10.1594/PANGAEA.887427.

References

Annan, J., & Hargreaves, J. (2013). A new global reconstruction of temperature changes at the Last Glacial Maximum. *Climate of the Past*, *9*(1), 367–376.

Armour, K. C., Bitz, C. M., & Roe, G. H. (2013). Time-varying climate sensitivity from regional feedbacks. *Journal of Climate*, *26*(13), 4518–4534.

Badger, M. P. S., Schmidt, D. N., Mackensen, A., & Pancost, R. D. (2013). High-resolution alkenone palaeobarometry indicates relatively stable pCO_2 during the Pliocene (3.3–2.8 Ma). *Philosophical Transactions of the Royal Society A*, *371*(2001), 20130094.

Bates, J. R. (2012). Climate stability and sensitivity in some simple conceptual models. *Climate Dynamics*, *38*(3–4), 455–473.

Bintanja, R., Fortuin, J. P. F., & Kelder, H. (1997). Simulation of the meridionally and seasonally varying climate response caused by changes in ozone concentration. *Journal of Climate*, *10*(6), 1288–1311.

Brovkin, V., Ganopolski, A., & Svirezhev, Y. (1997). A continuous climate-vegetation classification for use in climate-biosphere studies. *Ecological Modelling*, *101*(2), 251–261.

Caballero, R., & Langen, P. L. (2005). The dynamic range of poleward energy transport in an atmospheric general circulation model. *Geophysical Research Letters*, *32*, L02705. https://doi.org/10.1029/2004GL021581

Claussen, M., Mysak, L., Weaver, A., Crucifix, M., Fichefet, T., Loutre, M.-F., et al. (2002). Earth system models of intermediate complexity: Closing the gap in the spectrum of climate system models. *Climate Dynamics*, *18*(7), 579–586. https://doi.org/10.1007/s00382-001-0200-1

Covey, C., Sloan, L. C., & Hoffert, M. I. (1996). Paleoclimate data constraints on climate sensitivity: The paleocalibration method. *Climatic Change*, *32*(2), 165–184.

Crucifix, M. (2006). Does the Last Glacial Maximum constrain climate sensitivity? *Geophysical Research Letters*, *33*, L18701. https://doi.org/10.1029/2006GL027137

De Boer, B., Lourens, L. J., & Van de Wal, R. S. W. (2014). Persistent 400,000-year variability of Antarctic ice volume and the carbon cycle is revealed throughout the Plio-Pleistocene. *Nature Communications*, *5*, 2999. https://doi.org/10.1038/ncomms3999

De Boer, B., Van de Wal, R. S. W., Bintanja, R., Lourens, L. J., & Tuenter, E. (2010). Cenozoic global ice-volume and temperature simulations with 1-D ice-sheet models forced by benthic $\delta^{18}O$ records. *Annals of Glaciology*, *51*(55), 23–33.

De Boer, B., Van de Wal, R. S. W., Lourens, L. J., Bintanja, R., & Reerink, T. J. (2013). A continuous simulation of global ice volume over the past 1 million years with 3-D ice-sheet models. *Climate Dynamics*, *41*(5-6), 1365–1384.

Dowsett, H., Robinson, M., Haywood, A. M., Salzmann, U., Hill, D., Sohl, L. E., et al. (2010). The PRISM3D paleoenvironmental reconstruction. *Stratigraphy*, *7*(2–3), 123–139.

Edwards, T. L., Crucifix, M., & Harrison, S. P. (2007). Using the past to constrain the future: How the palaeorecord can improve estimates of global warming. *Progress in Physical Geography*, *31*(5), 481–500.

Friedrich, T., Timmermann, A., Tigchelaar, M., Timm, O. E., & Ganopolski, A. (2016). Non-linear climate sensitivity and its implications for future greenhouse warming. *Science Advances*, *2*(11). https://doi.org/10.1126/sciadv.1501923

Ganopolski, A., & Calov, R. (2011). The role of orbital forcing, carbon dioxide and regolith in 100 kyr glacial cycles. *Climate of the Past*, *7*(4), 1415–1425.

Ganopolski, A., Petoukhov, V., Rahmstorf, S., Brovkin, V., Claussen, M., Eliseev, A., & Kubatzki, C. (2001). CLIMBER-2: A climate system model of intermediate complexity. Part II: Model sensitivity. *Climate Dynamics*, *17*(10), 735–751.

Ganopolski, A., Winkelmann, R., & Schellnhuber, H. J. (2016). Critical insolation–CO_2 relation for diagnosing past and future glacial inception. *Nature*, *529*(7585), 200–203.

Goldner, A., Herold, N., & Huber, M. (2014). The challenge of simulating the warmth of the mid-Miocene climatic optimum in CESM1. *Climate of the Past*, *10*(2), 523–536. https://doi.org/10.5194/cp-10-523-2014

Hansen, J., Sato, M. K. I., Ruedy, R., Nazarenko, L., Lacis, A., Schmidt, G. A., et al. (2005). Efficacy of climate forcings. *Journal of Geophysical Research*, *110*, D18104. https://doi.org/10.1029/2005JD005776

Hargreaves, J. C., Annan, J. D., Yoshimori, M., & Abe-Ouchi, A. (2012). Can the Last Glacial Maximum constrain climate sensitivity? *Geophysical Research Letters*, *39*, L24702. https://doi.org/10.1029/2012GL053872

Haywood, A. M., Hill, D. J., Dolan, A. M., Otto-Bliesner, B. L., Bragg, F., Chan, W.-L., et al. (2013). Large-scale features of Pliocene climate: Results from the Pliocene Model Intercomparison Project. *Climate of the Past*, *9*, 191–209.

Holland, M. M., & Bitz, C. M. (2003). Polar amplification of climate change in coupled models. *Climate Dynamics*, *21*(3–4), 221–232.

Ivanovic, R. F., Gregoire, L. J., Roche, D. M., Valdes, P. J., & Peltier, W. R. (2016). Transient climate simulations of the deglaciation 21-9 thousand years before present (version 1)—PMIP4 Core experiment design and boundary conditions. *Geoscientific Model Development*, *9*(7), 2563–2587.

Jouzel, J., Masson-Delmotte, V., Cattani, O., Dreyfus, G., Falourd, S., Hoffmann, G., et al. (2007). Orbital and millennial Antarctic climate variability over the past 800,000 years. *Science*, *317*(5839), 793–796.

Kohfeld, K. E., & Harrison, S. P. (2001). DIRTMAP: The geological record of dust. *Earth-Science Reviews*, *54*(1), 81–114.

Köhler, P., Bintanja, R., Fischer, H., Joos, F., Knutti, R., Lohmann, G., & Masson-Delmotte, V. (2010). What caused Earth's temperature variations during the last 800,000 years? Data-based evidence on radiative forcing and constraints on climate sensitivity. *Quaternary Science Reviews*, *29*(1), 129–145.

Köhler, P., de Boer, B., Von der Heydt, A. S., Stap, L. B., & Van de Wal, R. S. W. (2015). On the state-dependency of the equilibrium climate sensitivity during the last 5 million years. *Climate of the Past*, *11*, 1801–1823.

Köhler, P., Stap, L. B., von der Heydt, A. S., de Boer, B., van de Wal, R. S. W., & Bloch-Johnson, J. (2017). A state-dependent quantification of climate sensitivity based on paleodata of the last 2.1 million years. *Paleoceanography*, *32*, 1102–1114. https://doi.org/10.1002/2017PA003190

Kutzbach, J. E., He, F., Vavrus, S. J., & Ruddiman, W. F. (2013). The dependence of equilibrium climate sensitivity on climate state: Applications to studies of climates colder than present. *Geophysical Research Letters*, *40*, 3721–3726. https://doi.org/10.1002/grl.50724

Lambert, F., Delmonte, B., Petit, J.-R., Bigler, M., Kaufmann, P. R., Hutterli, M. A., et al. (2008). Dust-climate couplings over the past 800,000 years from the EPICA Dome C ice core. *Nature*, *452*(7187), 616–619.

Laskar, J., Robutel, P., Joutel, F., Gastineau, M., Correia, A. C. M., Levrard, B., et al. (2004). A long-term numerical solution for the insolation quantities of the Earth. *Astronomy & Astrophysics*, *428*(1), 261–285.

Lisiecki, L. E., & Raymo, M. E. (2005). A Pliocene-Pleistocene stack of 57 globally distributed benthic $\delta^{18}O$ records. *Paleoceanography*, *20*, PA1003. https://doi.org/10.1029/2004PA001071

Lunt, D. J., Dunkley Jones, T., Heinemann, M., Huber, M., LeGrande, A., Winguth, A., et al. (2012). A model–data comparison for a multi-model ensemble of early Eocene atmosphere–ocean simulations: EoMIP. *Climate of the Past*, *8*, 1717–1736.

Mahowald, N. M., Muhs, D. R., Levis, S., Rasch, P. J., Yoshioka, M., Zender, C. S., & Luo, C. (2006). Change in atmospheric mineral aerosols in response to climate: Last glacial period, preindustrial, modern, and doubled carbon dioxide climates. *Journal of Geophysical Research*, *111*, D10202. https://doi.org/10.1029/2005JD006653

Martínez-Botí, M. A., Foster, G. L., Chalk, T. B., Rohling, E. J., Sexton, P. F., Lunt, D. J., et al. (2015). Plio-Pleistocene climate sensitivity evaluated using high-resolution CO_2 records. *Nature*, *518*(7537), 49–54.

Masson-Delmotte, V., Kageyama, M., Braconnot, P., Charbit, S., Krinner, G., Ritz, C., et al. (2006). Past and future polar amplification of climate change: Climate model intercomparisons and ice-core constraints. *Climate Dynamics*, *26*(5), 513–529.

Meraner, K., Mauritsen, T., & Voigt, A. (2013). Robust increase in equilibrium climate sensitivity under global warming. *Geophysical Research Letters*, *40*, 5944–5948. https://doi.org/10.1002/2013GL058118

Myhre, G., Highwood, E. J., Shine, K. P., & Stordal, F. (1998). New estimates of radiative forcing due to well mixed greenhouse gases. *Geophysical Research Letters*, *25*(14), 2715–2718.

PALAEOSENS Project Members (2012). Making sense of palaeoclimate sensitivity. *Nature*, *491*(7426), 683–691.

Petoukhov, V., Ganopolski, A., Brovkin, V., Claussen, M., Eliseev, A., Kubatzki, C., & Rahmstorf, S. (2000). CLIMBER-2: A climate system model of intermediate complexity. Part I: Model description and performance for present climate. *Climate Dynamics*, *16*(1), 1–17.

Pfister, P. L., & Stocker, T. F. (2017). State-dependence of the climate sensitivity in Earth System Models of intermediate complexity. *Geophysical Research Letters*, *44*, 10,643–10,653. https://doi.org/10.1002/2017GL075457

Robinson, A., Calov, R., & Ganopolski, A. (2011). Greenland ice sheet model parameters constrained using simulations of the Eemian Interglacial. *Climate of the Past*, *7*(2), 381–396.

Romanova, V., Lohmann, G., Grosfeld, K., & Butzin, M. (2006). The relative role of oceanic heat transport and orography on glacial climate. *Quaternary Science Reviews*, *25*(7), 832–845.

Schmittner, A., Urban, N. M., Shakun, J. D., Mahowald, N., Clark, P. U., Bartlein, P. J., et al. (2011). Climate sensitivity estimated from temperature reconstructions of the Last Glacial Maximum. *Science*, *334*(6061), 1385–1388. https://doi.org/10.1126/science.1203513

Schneider von Deimling, T., Held, H., Ganopolski, A., & Rahmstorf, S. (2006). Climate sensitivity estimated from ensemble simulations of glacial climate. *Climate Dynamics*, *27*(2–3), 149–163.

Shakun, J. D. (2017). Modest global-scale cooling despite extensive early Pleistocene ice sheets. *Quaternary Science Reviews*, *165*, 25–30.

Singarayer, J. S., & Valdes, P. J. (2010). High-latitude climate sensitivity to ice-sheet forcing over the last 120 kyr. *Quaternary Science Reviews*, *29*(1), 43–55.

Snyder, C. W. (2016). Evolution of global temperature over the past two million years. *Nature*, *538*(7624), 226–228.

Stap, L. B., de Boer, B., Ziegler, M., Bintanja, R., Lourens, L. J., & van de Wal, R. S. W. (2016). CO_2 over the past 5 million years: Continuous simulation and new $\delta^{11}B$-based proxy data. *Earth and Planetary Science Letters*, *439*, 1–10.

Stap, L. B., van de Wal, R. S. W., de Boer, B., Bintanja, R., & Lourens, L. J. (2017). The influence of ice sheets on temperature during the past 38 million years inferred from a one-dimensional ice sheet–climate model. *Climate of the Past*, *13*(9), 1243–1257. https://doi.org/10.5194/cp-13-1243-2017

Stein, U., & Alpert, P. (1993). Factor separation in numerical simulations. *Journal of the Atmospheric Sciences*, *50*(14), 2107–2115.

Stocker, T. F., Mysak, L. A., & Wright, D. G. (1992). A zonally averaged, coupled ocean-atmosphere model for paleoclimate studies. *Journal of Climate*, *5*(8), 773–797.

Stuber, N., Ponater, M., & Sausen, R. (2005). Why radiative forcing might fail as a predictor of climate change. *Climate Dynamics*, *24*(5), 497–510.

Van de Wal, R. S. W., de Boer, B., Lourens, L. J., Köhler, P., & Bintanja, R. (2011). Reconstruction of a continuous high-resolution CO_2 record over the past 20 million years. *Climate of the Past*, *7*(4), 1459–1469. https://doi.org/10.5194/cp-7-1459-2011

Vial, J., Dufresne, J.-L., & Bony, S. (2013). On the interpretation of inter-model spread in CMIP5 climate sensitivity estimates. *Climate Dynamics*, *41*(11–12), 3339–3362.

Von der Heydt, A. S., Dijkstra, H. A., van de Wal, R. S. W., Caballero, R., Crucifix, M., Foster, G. L., et al. (2016). Lessons on climate sensitivity from past climate changes. *Current Climate Change Reports*, *2*(4), 148–158.

Von der Heydt, A. S., Köhler, P., Van de Wal, R. S. W., & Dijkstra, H. A. (2014). On the state dependency of fast feedback processes in (paleo) climate sensitivity. *Geophysical Research Letters*, *41*, 6484–6492. https://doi.org/10.1002/2014GL061121

Willeit, M., Ganopolski, A., Calov, R., Robinson, A., & Maslin, M. (2015). The role of CO_2 decline for the onset of Northern Hemisphere glaciation. *Quaternary Science Reviews*, *119*, 22–34.

Yoshimori, M., Hargreaves, J. C., Annan, J. D., Yokohata, T., & Abe-Ouchi, A. (2011). Dependency of feedbacks on forcing and climate state in physics parameter ensembles. *Journal of Climate*, *24*(24), 6440–6455.